Springer

KSME

Journal of Mechanical Science and Technology 24 (10) (2010) 1~10
www.springerlink.com/content/1738-494x
DOI 10.1007/s12206-010-0712-x

Investigating flow patterns in a channel with complex obstacles using the lattice Boltzmann method

Jiraporn Yojina[1,2], Waipot Ngamsaad[2], Narin Nuttavut[2], Darapond Triampo[2,5], Yongwimon Lenbury[1], Paisan Kanthang[6], Somchai Sriyab[1,2] and Wannapong Triampo[2,3,4,*]

[1]*Mathematics Department, Center of Excellence in Mathematics, Faculty of Science, Mahidol University, Rama VI, Bangkok, Thailand 10400*
[2]*Biophysics Group, Department of Physics, Faculty of Science, Mahidol University, Rama VI, Bangkok, Thailand 10400*
[3]*Center of Excellence for Vectors and Vector-Borne Diseases, Faculty of Science, Mahidol University, Rama VI, Bangkok, Thailand 10400*
[4]*ThEP Center, CHE, 328 Si Ayutthaya Road, Bangkok, Thailand 10400*
[5]*Department of Chemistry, Center of Excellence for Innovation in Chemistry, Faculty of Science, Mahidol University, Rama VI, Bangkok, Thailand 10400*
[6]*Rajamangala University of Technology, Phra Nakhon, Bangkok, Thailand 10800*

(Manuscript Received October 14, 2009; Revised May 1, 2010; Accepted June 28, 2010)

Abstract

In this work, mesoscopic modeling via a computational lattice Boltzmann method (LBM) is used to investigate the flow pattern phenomena and the physical properties of the flow field around one and two square obstacles inside a two-dimensional channel with a fixed blockage ratio, $\beta = 1/4$, centered inside a 2D channel, for a range of Reynolds numbers (Re) from 1 to 300. The simulation results show that flow patterns can initially exhibit laminar flow at low Re and then make a transition to periodic, unsteady, and, finally, turbulent flow as the Re get higher. Streamlines and velocity profiles and a vortex shedding pattern are observed. The Strouhal numbers are calculated to characterize the shedding frequency and flow dynamics. The effect of the layouts or configurations of the obstacles are also investigated, and the possible connection between the mixing process and the appropriate design of a chemical mixing system is discussed.

Keywords: Flow pattern; Lattice Boltzmann method; Strouhal number; Von Karman vortex street

1. Introduction

There is keen interest in chemical mixing fluidic devices, especially to improving the efficacy of the mixing. Y-channel is a well known prototype of the binary mixer for two material species.

An illustrative example is shown in Fig. 1, where a flow channel with obstacles of two rows of samples is met, combined, and then pushed out through a Y-shaped channel on a chip. Mixing a system purely by moving the samples through specific channel geometries occurs via one of the most fundamental principles of physics, and utilizes the manipulation of obstacle configurations.

As a multidisciplinary problem, there is an array of scientific and mathematical tools available to begin addressing it. With our background in computational physics, we chose to use mesoscopic modeling via the computational lattice Boltzmann method (LBM) in order to gain further insight into flow properties and patterns. To our knowledge, this is the first investigation into this system (with these obstacle configurations) that uses this approach. As a first step to a more compli-

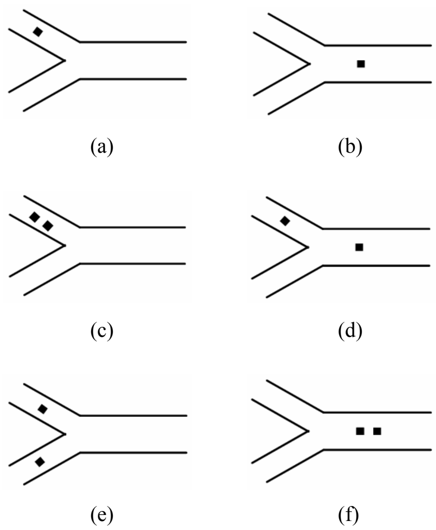

Fig. 1. Evolution of design with square obstacle in the Y-channel.

† This paper was recommended for publication in revised form by Associate Editor Jun Sang Park

*Corresponding author. Tel.: +662-441-9816, Fax: +662-441-9322
E-mail address: wtriampo@gmail.com, scwtr@mahidol.ac.th

cated model, we started with a simple but still relevant model: a small channel flow with complex obstacles. We hypothesized that the turbulent pressure produced by the obstacles could be managed to increase the efficacy of the mixing. Since our focused systems are generally operated at low Reynolds numbers, it seemed sensible to use obstacles as "catalysts" to generate unsteady or turbulent flow. Our primary goal was to investigate the flow pattern and properties in order to provide a framework for assisting applied design-making.

For example, Davis *et al.* [1] investigated a confined flow passing a square cylinder for a wide range of Reynolds numbers (Re) with two different blockage ratios ($1/6, 1/4$); the ratio between the size of the obstacle and the channel height were defined as β, experimentally and numerically. Mukhopadhyay *et al*. [2] and Suzaki *et al.* [3] also carried out 2D numerical simulations over a wide range of Re, with the range of blockage ratio being $1/8-1/4$. Breuer *et al.* used the LBM and the finite-element method (FEM) in their analysis for a fixed blockage ratio $\beta = 1/8$ in the range $0.5 \le \mathrm{Re} \le 300$. Bin *et al.* [4] investigated the dynamical behavior of the flow and the topology of the vortex structure behind a square cylinder in a 2D duct with blockage ratio $\beta = 1/8$. In the same year, Ratanadecho [5] performed a 2D flow around an arbitrary obstacle in a channel by using the LBM. Carmo *et al.* [6] employed the FEM to investigate the incompressible flow around pairs of circular cylinders in tandem arrangements. Lastly, Islam *et al.* [7] used the LBM to describe their numerical study of flow past a row of circular cylinders.

Despite the informative findings from all this previous research, more work still needs to be done—for slight differences in set-ups or parameters can produce immense differences. In addition, the understanding of flow past a square and two square obstacles is quite limited because numerical simulations are still relatively rare. Therefore, in our current study we employed the LBM as an efficient numerical tool for simulating fluid and transport based on kinetic equations and statistical physics [8-11], in order to investigate the flow pattern phenomena and the topology of vortex shedding behind one and two square obstacles with a fixed blockage ratio, $\beta = 1/4$, centered inside a 2D channel for a range of Re from 1 to 300. Moreover, we studied the effect of the layout of the obstacle in the flow past two square obstacles versus one square obstacle.

2. Lattice Boltzmann method

The lattice Boltzmann method (LBM) is a numerical scheme which evolved from the lattice gas model (LGM) [12, 13]. The LGM is a method to determine the kinetics of particles by utilizing a discrete lattice and discrete time. It has provided insights into the underlying microscopic dynamics of a physical system, while most other methods focus only on the solution of the macroscopic equation. However, the particles in the LGM obey an exclusion principle that has microscopic collision rules. These rules require many random numbers that create noise or fluctuations. Moreover, LGM is very complicated. An ensemble averaging requires that the noise be smoothed out in order to obtain the macroscopic dynamics. The LGM collects the behavior of the microscopic particles in the system that are not sensitive to the underlying details at the microscopic level. It also leads to an increase in the amount of computational storage required, which in turn leads to a reduction in the computational speed. For these reasons, the LBM is interested in the evolution of averaged quantities and not the influence of the fluctuations [12]. It is relatively easy with the LBM to implement a more complex boundary condition, such as the curved boundary [14], when compared to conventional grid-based numerical integration. In addition, the LBM algorithm is greatly beneficial in terms of simulating time in a straight forward manner for complex geometry and parallel computing [15].

Traditional computational methods in fluid dynamics (such as the finite element method, finite difference method, and finite volume method) solve macroscopic fluid dynamics equations, while the LBM solves a problem at the microscopic level in order to recover particle's density and velocity from its macroscopic properties [16]. The microscopic particle distribution function evolves at each time step through two sequential sub-steps: propagation and collision. In the first step, propagation (or streaming), the particles from one lattice site move to its nearest lattice site along the direction of their velocity. During the second step, collision, various interactions among particles are imitated according to scattering rules by allowing for the relaxation of a distribution toward an equilibrium distribution through a linear relaxation parameter.

The lattice Boltzmann equation can be viewed as a discrete form of the continuous Boltzmann BGK model [9, 17], which is given by:

$$f_\alpha(\vec{x}_\alpha + \vec{e}_\alpha \delta t, t + \delta t) - f_\alpha(\vec{x}_\alpha, t) = \frac{-1}{\tau}(f_\alpha - f_\alpha^{eq}) \tag{1}$$

where $f_\alpha \equiv f_\alpha(\vec{x}_\alpha, t)$ is the distribution function at space $\vec{x}_\alpha$ and where time t associated with the discrete velocity $\vec{e}_\alpha$ in which the particle distribution moves to the next lattice node in one time step δt, $\tau = \lambda / \delta t$ is the dimensionless relaxation time.

In this lattice BGK (LBGK) model, the structure is generally referred to as $DnQm$ for n (microscopic) velocity models in m directions. The numerical simulations in this research are based on a $D2Q9$ lattice structure, since it has been widely and successfully used for simulating $2D$ flows, as seen in Fig. 2.

In LBM, the space is divided into a regular Cartesian lattice grid, as a consequence of the symmetry of the discrete velocity set. Each lattice site is shown with the rest particle at the center and eight further lattice links along which particles can propagate with two different speeds, depending on whether they move diagonally or along the compass directions and where $\vec{e}_\alpha$ denotes the discrete velocity set, expressed as:

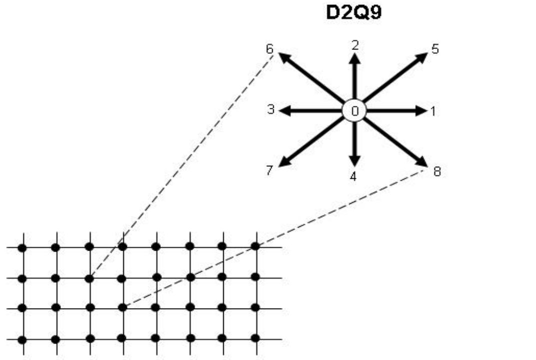

Fig. 2. A two-dimensional nine-velocity lattice structure (D2Q9 model).

$$\vec{e}_\alpha = \begin{cases} (0,0), & \alpha = 0, \\ c(\cos\theta_\alpha, \sin\theta_\alpha),\ \theta_\alpha = (\alpha-1)\pi/2, & \alpha = 1,2,3,4, \\ \sqrt{2}c(\cos\theta_\alpha, \sin\theta_\alpha),\ \theta_\alpha = (\alpha-5)\pi/2 + \pi/4, \\ \alpha = 5,6,7,8 \end{cases} \quad (2)$$

where $c = \delta x/\delta t$. The equilibrium distribution function is written as:

$$f_\alpha^{eq} = \omega_\alpha \rho \left(1 + 3\vec{e}_\alpha \cdot \vec{u} + \frac{9(\vec{e}_\alpha \cdot \vec{u})^2}{2} - \frac{3u^2}{2} \right). \quad (3)$$

The weighting factor ω_α is given by:

$$\omega_\alpha = \begin{cases} 4/9, & \alpha = 0, \\ 1/9, & \alpha = 1,2,3,4, \\ 1/36, & \alpha = 5,6,7,8 \end{cases} \quad (4)$$

The macroscopic density ρ per node and velocity $\vec{u} = (u,v)$ are recovered from the particle distribution according to summations over the lattice links:

$$\rho = \sum_\alpha f_\alpha ,$$
$$\rho\vec{u} = \sum_\alpha e_\alpha f_\alpha .$$

Eq. (1) is referred to as the LBE with BGK approximation, or the LBGK model, which is currently the most widely used model. It is usually solved in the following two steps, which occur in one time step δt:

Collision step:
$$\tilde{f}_\alpha(\vec{x}_\alpha, t+\delta t) = f_\alpha(\vec{x}_\alpha, t) - \frac{1}{\tau}(f_\alpha(\vec{x}_\alpha, t) - f_\alpha^{eq}(\vec{x}_\alpha, t)) \quad (5)$$

Streaming step: $f_\alpha(\vec{x}_\alpha + \vec{e}_\alpha \delta t, t+\delta t) = \tilde{f}_\alpha(\vec{x}_\alpha, t+\delta t)$ (6)

For the simulation algorithm, it consists of two steps that are repeated in each time step, which are the streaming step and collision step. In the first step, the actual movement of the particles takes place throughout the grid. The second step accounts for the collision changes due to the movement of particles which changes the distribution of the particles for all distribution. For most time steps, we firstly determine the density ρ and the velocity $\vec{u}$; then f^{eq} is calculated. The algorithm via the flowchart diagram is shown in Fig. 3.

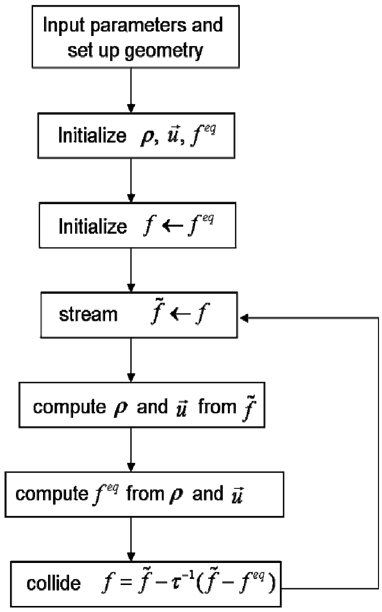

Fig. 3. Flowchart diagram.

By applying the Chapman-Enskog analysis, or multiscale analysis, we take the Taylor expansion of LBM in Eq. (1), then we may deduce:

$$\begin{aligned} f_\alpha(\vec{x} + c_\alpha \delta_t, t+\delta_t) &= \sum_{n=0}^{\infty} \frac{\varepsilon^n}{n!} D_t^n f_\alpha(\vec{x}, t) \\ &= f_\alpha(\vec{x}, t) + \varepsilon(\partial_t + c_\alpha \cdot \nabla) f_\alpha(\vec{x}, t) \\ &\quad + \frac{\varepsilon^2}{2}(\partial_t + c_\alpha \cdot \nabla)^2 f_\alpha(\vec{x}, t) + \ldots \end{aligned} \quad (7)$$

We arrange Eq. (7) in terms of the Knudsen number (ε), which becomes:

$$f_\alpha = f_\alpha^{(0)} + \varepsilon f_\alpha^{(1)} + \varepsilon^2 f_\alpha^{(2)} + O(\varepsilon^3) \quad (8)$$
$$\frac{\partial}{\partial t} = \varepsilon \frac{\partial}{\partial t_1} + \varepsilon^2 \frac{\partial}{\partial t_2} \quad (9)$$
$$\nabla = \varepsilon \nabla_1 \quad (10)$$

where $f^{(0)} = f^{eq}$. We assume that the diffusion time scale t_2 is much smaller than the convection time scale t_1. Eqs. (6)-(8) satisfy the constraints:

$$\sum_\alpha f_\alpha^{(0)} = \rho, \quad (11)$$

$$\sum_{\alpha} e_{\alpha} f_{\alpha}^{(0)} = \rho \vec{u}, \tag{12}$$

Finally, we obtain the isothermal Navier-Stokes equations in the incompressible limit and by neglecting any body forces as:

$$\nabla \cdot \vec{u} = 0 \quad , \tag{13}$$

$$\partial_t \vec{u} + (\vec{u} \cdot \nabla)\vec{u} = \frac{-1}{\rho} \nabla p + \upsilon \nabla^2 \vec{u} \ , \tag{14}$$

where $\upsilon = \frac{(2\tau - 1)}{6} \frac{(\delta x)^2}{\delta t}$ (15)

and $p = \rho c_s^2$ where $c_s^2 = c \big/ \sqrt{3}$ is the speed of sound in this model, υ is the viscosity, and p is the pressure.

3. Simulate configurations and measurements

In this research, we study the 2D flow around one and two square obstacles with diameter d, centered inside a plane channel (height H, length L). The inflow length is l and the distance between two square obstacles is $l_0 = nd$, where $n = 5,10,15$ are simulated numerically on an $Nx \times Ny$ lattice for $1 \le \mathrm{Re} \le 300$. The computational domains are shown in Fig. 4. The blockage ratio, $\beta = d/H$, is fixed at $\beta = 1/4$.

The dimensionless equations for continuity and momentum may be expressed as:

$$\nabla \cdot \vec{u} = 0 \ , \tag{16}$$

$$\frac{\partial \vec{u}}{\partial t} + (\vec{u} \cdot \nabla)\vec{u} = -\nabla p + \frac{1}{\mathrm{Re}} \nabla^2 \vec{u} \ , \tag{17}$$

where $\mathrm{Re} = \frac{u_{\max} d}{\upsilon}$, $u_{\max}$ is the maximum flow velocity of the parabolic inflow profile and υ is the kinematic viscosity. In the simulation, we use the parameters as shown in Table. 1.

For the boundary condition, we generalize into two branches: a solid wall boundary and an open boundary condition, such as inlet/outlet channels. For the solid wall boundary condition, we use the most popular no-slip boundary condition, Bounce-Back [13], due to its ease of implementation. The solid wall lies exactly at the lattice nodes and it is assumed that all particles entering the boundary node leave with the same magnitude of speed but in the opposite direction of their incoming velocities (see Fig. 5). For the open boundary, it is common to assign a given velocity profile to the fluid inlet, while either a given pressure or zero normal velocity gradient is assigned to the outlet. It is noted that the boundaries of the block coincide exactly with the lattice points. This original bounce-back scheme is only of first order in numerical accuracy at boundaries. The original bounce-back scheme is simple but cannot guarantee higher accuracy on the boundary. To overcome this low numerical accuracy, two other approaches tackle complex geometries more directly and have significant impact on second order accuracy: (i) interpolated bounce-back approaches and their generalization as a multi-reflection boundary scheme (ii) volumetric bounce-back scheme.

Table 1. All parameters in the simulations.

N_x	Number of grids in x direction	250 (I) 500 (II)
N_y	Number of grids in y direction	41
d	Size of the obstacle	10
$u_{\max}$	The maximum velocity of inflow	0.02
β	The blockage ration	¼
l	Inflow length	50
$l_0 = nd$, n=5, 10, 15	Distance between two obstacles	50, 100, 150

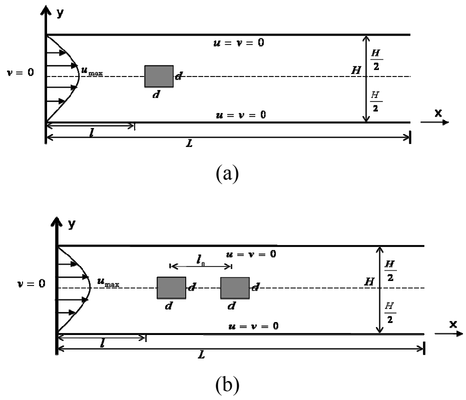

(a)

(b)

Fig. 4. (a) The geometry and domain for a square obstacle (b) The geometry and domain for two square obstacles.

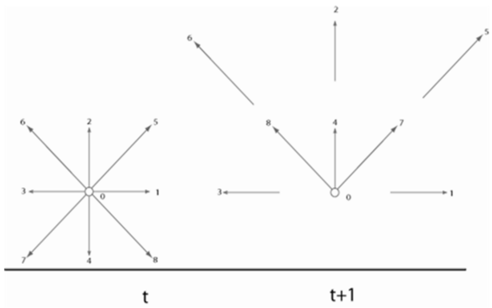

Fig. 5. Bounce-back boundary condition.

So the choice of the original bounce-back made in the present work is mainly due to simplicity.

For the simulation, we implement our LBM algorithm for Eqs. (5)-(6) and visualize the output data by using Matlab code. At an instant of time, the streamlines [18] are calculated to represent the flow velocity field of fluid, which is defined as:

$$\frac{d\vec{x}_s}{ds} \times \vec{u}(\vec{x}_s) = 0 \tag{18}$$

where $\vec{u} = (u, v)$ is the local velocity vector and those of the streamline are $\vec{x}_s = (x_s, y_s)$. We then can deduce:

$$\frac{dx_s}{u} = \frac{dy_s}{v} \tag{19}$$

where the curves are parallel to the velocity vector.

To characterize the flow pattern, one important quantity taken into account in the present analysis is the Strouhal number, St : a dimensionless number describing oscillating flow mechanisms. It is computed from the obstacle size d , the measured frequency of the vortex shedding f , and the maximum velocity $u_{\max}$, at the inflow, and is defined as:

$$St = \frac{fd}{u_{\max}} . \tag{20}$$

The characteristic frequency f is determined by a spectral analysis (fast Fourier transform, FFT [14]) of the time series of the temporal evolution of the u-component of flow velocity at several points in the wake behind the obstacle, ranging from 512-1024 points.

4. Validation of the simulation and the accuracy test

To verify the accuracy of our simulations, we compared the results from our LBM model with the analytic solution for plane channel Poiseuille flow in the y-direction, i.e., zero vertical velocity (see Fig. 4). This analytical solution is given by:

$$u_j = \frac{4U_c}{n^2} j(n-j), \quad j = 1,\ldots,n-1 . \tag{21}$$

where $U_c = \frac{L_y^2 G}{8\upsilon}$ is the centerline velocity without slips at boundaries, with $L_y = n\delta_x$ being the width of the channel and $G = \frac{\Delta p}{\rho L_x}$. The velocity profile from Eq. (21) is a perfect parabola as shown in Fig. 6. We carried out two simulations, one with 80 grid points in the y-direction and one with 40 grid points. For both simulations we used 250 grid points in the x-direction. In each of our simulations, we assumed that the initial state is given by zero velocity vector and we used the boundary condition for a stationary wall, i.e., the bounce-back rule. In both simulations, we measured u at the cross section of the channel after 10000 time steps (iterations). We found that the velocity profiles from both situations were parabolic, although the velocity profiles corresponding to the area around the center of channel were slightly different from the analytic solution. This might be due to the effect of our computation of initial fluid densities from the Maxwell-Boltzmann equilibrium distribution. The simulation results give a perfect parabola for the velocity profiles and do not show any effect from the no-slip velocity boundary condition at the wall or from the grid resolution. In addition the numerical results are consistent with the analytical solution in Eq. (21).

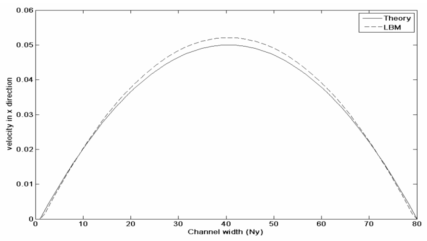

(a)

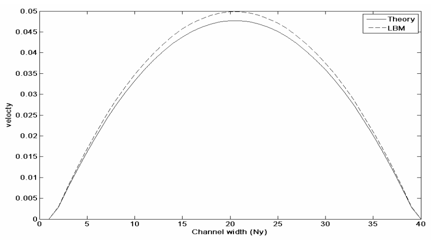

(b)

Fig. 6. The comparison of the velocity profiles between analytic solution of the Poiseuille flow and our simulation (LBM) results, (a) the channel width $(Ny = 80)$ and (b) the channel width $(Ny = 40)$.

5. Results and discussion

The simulation was performed numerically for a range of Re numbers between 1 and 300. For all cases considered, the size of the obstacle $d \times d = 10 \times 10$ in the lattice unit was positioned at $l = 50$ in the lattice downstream from the entrance of the channel and was simulated at 100,000 iterations. The following section starts with a description of the different flow patterns (as shown by the streamline plot and velocity profile) with increasing Re . Furthermore, the computations analyze the St to specify the characteristic of the flow pattern behind the obstacle.

5.1 Flow pattern around a square obstacle

The flow around a square obstacle positioned inside a channel where $\mathrm{Re} = 1$ was simulated first. According to the computational domain as shown in Fig. 4(a), we used the obstacle size $d = 10$ lattice units. The streamline contours and velocity profiles for various Re numbers, as shown in Fig. 7 and Fig. 8, respectively, were employed to demonstrate the flow phenomena. We found that the creeping steady flow around a square obstacle persists without separation for $\mathrm{Re} \approx 1$, as shown in Fig. 7(a). For $30 < \mathrm{Re} < 85$, the flow pattern is firstly separated at the trailing edge of the obstacle, and the length of the recirculation region increases linearly with Re , as is clearly seen in Fig. 7(b)-(c). These results are perfectly symmetric with respect to the oncoming flow and the vortex shedding which has not yet started. When increasing Re , the symmetry eventually breaks down and becomes unstable, as shown in Fig. 7(d)-(h).

In our observations, the laminar flow changed to an unstable flow at around $\mathrm{Re} \approx 85$, which is called the critical Re

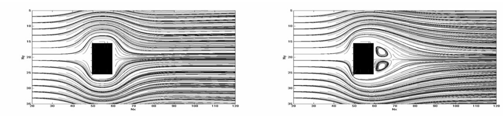

(a) Re=1 (b) Re=30

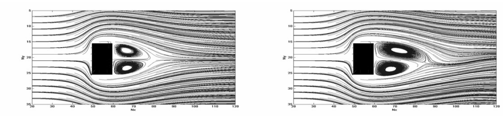

(c) Re=60 (d) Re=85

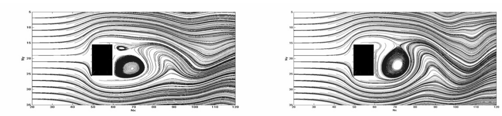

(e) Re=100 (f) Re=160

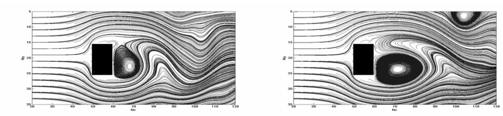

(g) Re=200 (h) Re=300

Fig. 7. Streamline plot around a square obstacle for different Reynolds numbers.

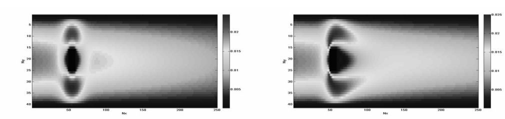

(a) Re=1 (b) Re=30

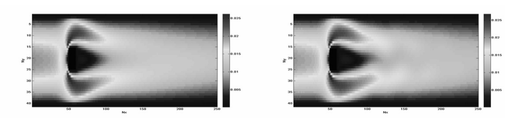

(c) Re=60 (d) Re=85

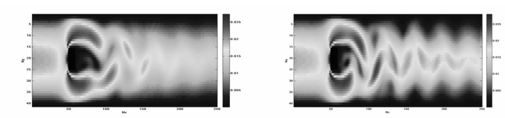

(e) Re=100 (f) Re=160

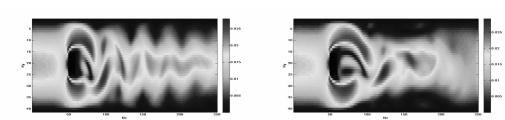

(g) Re=200 (h) Re=300

Fig. 8. Velocity profiles around a square obstacle for different Reynolds numbers.

(Re_{crit}). We found that the Re_{crit} is greater than that of Bin et al. [10] and Breuer et al. [4] due to the differences in the flow parameters, such as the blockage ratio and the input flow velocity. These results are supported by the visualization of the flow velocity profiles in Fig. 8. For $Re < Re_{crit}$, the velocity profiles present the laminar flow as shown in Fig. 8(a)-(c). According to the asymmetry of the flow pattern and a sufficient number of iterations, these flows become periodic and

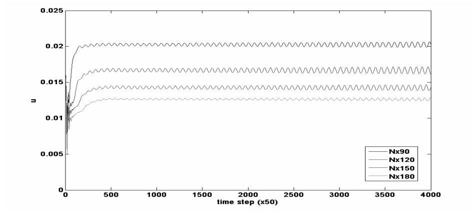

(a) Re=85

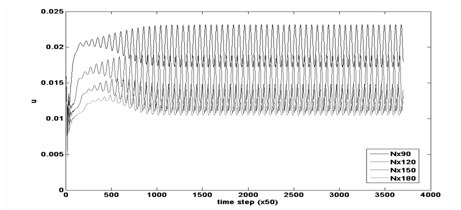

(b) Re=100

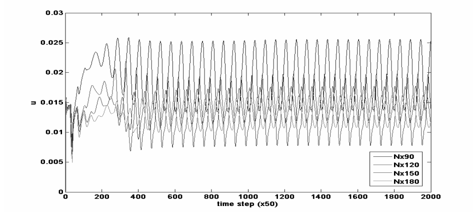

(c) Re=160

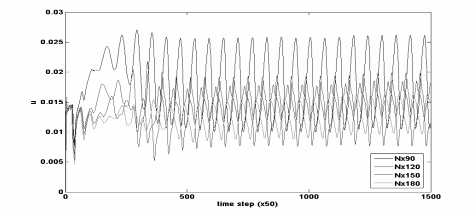

(d) Re=200

Fig. 9. Time series of the flow velocity for one obstacle at several positions for Reynolds numbers Re=85,100,160,200.

alternate the shedding of vortices into the stream, as shown in Fig. 8(d)-(h). This is known as a von Karman vortex street, which exhibits an unstable flow pattern and performs a shedding pattern behind the obstacle. For $Re > 260$, the periodic pattern is lost and there is no steady solution (see in Fig. 8(h)).

To see how the measuring position affects the periodic flow pattern, we collected the time series data of the velocity profile behind the obstacle at various positions ($Nx = 90,120,150,180$), as shown in Fig. 9. It was noticed that the position close to the obstacle generates periodic patterns more quickly than other positions and the amplitudes of these time series data seem to decrease as the position recedes far away from the obstacle. In the wake behind the obstacle $(\approx 1\%)$, we found that the frequency values are nearly independent of the position. In practice, there is no definite criterion where to choose a position far away from the obstacle. So we chose a position near the obstacle to clearly demonstrate the shedding pattern and represent the frequency at each Re.

For more quantitative analysis, we used the St to charac-

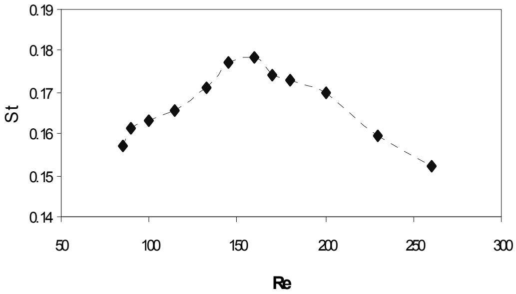

Fig. 10. Strouhal number of the vortex shedding pattern for the flow around one obstacle for a range of Reynolds numbers $85 \le \mathrm{Re} \le 260$.

terize the shedding pattern, as shown in Eq. (20). First, we calculated the frequency of the shedding pattern by using the FFT of the time series data of the flow velocity as presented in Fig. 9. The St was calculated for a range of Re , the results of which are shown in Fig. 10. When the Re increased, the St also increased until reaching the maximum. The Re for the maximum St is around 160. After St is at maximum, it decreases when Re increases. This result corresponds to the finding of Bin *et al.* [10]. They provided a local maximum of St at $\mathrm{Re} \approx 160$ for the blockage ratio $\beta = 1/8$, and showed that St has no effect on the grid resolution. However, their St values are slightly lower than the results in the present work ($\beta = 1/4$) because of the increased blockage ratio [5].

We want to mention that depending on the Reynolds number (Re) , various types of flow regimes can be distinguished for the flow past buff bodies. At low Re , the flow shows a steady flow when a critical Reynolds number (Re_{crit}) is exceeded, and the von Karman vortex street with periodic vortex shedding can be detected in the wake. The vortices appear and are shed alternatively at a constant frequency which where the frequency increases as increasing Re . About $\mathrm{Re} \approx 160$, the structure of the von Karman vortex street becomes three-dimensional (3D) which is due to lower frequency as further Re increases. These results are consistent with the circular cylinder flow for which Williamson (1996) [19] which he provides a Re limit of $\mathrm{Re} \approx 180$ for the onset of 3D structure in the wake. Beyond this limit 3D structure limits, the Strouhal number value decreases with increasing Reynolds number at $\mathrm{Re} > 160$. We may physically interpret research findings as follows. Since the Strouhal number is a dimensionless value useful for analyzing oscillating unsteady fluid flow dynamics (which is proportional to oscillation frequency and inversely proportional to the flow velocity), then the St is increased early on according to the increase in Re. However, as being pointed out after reaching some Re value (about 160), the dynamics does change to become less oscillating resulting in less frequency observed. Hence the frequency velocity ratio is smaller and so is St . In addition, because St represents a measure of the ratio of inertial forces due to the unsteadiness of the flow or the local acceleration to the inertial forces due to changes in velocity from one point to another in the flow field, this is the case for the situation for $\mathrm{Re} < 160$. Yet, for $\mathrm{Re} > 160$ once again the structure of a von Karman vortex street becomes three-dimensional (3D), which is due to lower frequency, and this causes the lowering in St .

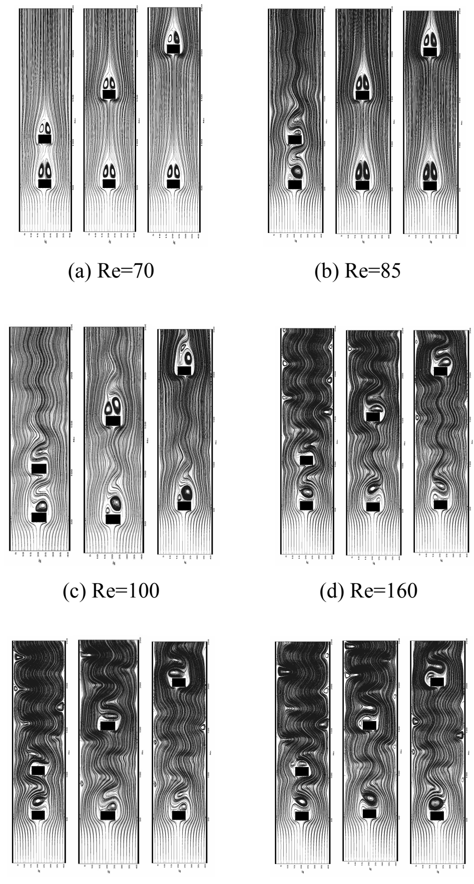

Fig. 11. Streamline plot around two square obstacles for Re=70,85,100,160,180,200 and various the distance l_0 i.e. $l_0 = 50$ (left), $l_0 = 100$ (middle) and $l_0 = 150$ (right).

5.2 Flow pattern around two square obstacles

For practical applications, we studied the flow pattern through two square obstacles inside the channel, on a 40×500 lattice with a fixed blockage ratio $\beta = 1/4$, and effected the flow by varying the distance between two square obstacles l_0 , $l_0 = nd$ where $n = 5,10,15$.

To illustrate the flow phenomena, we present the characterization of the flow pattern via the streamline and velocity profile, as shown in Fig. 11 and 12. For the streamline, the flow field of low Re (for example, $\mathrm{Re} = 70$) separates at the edge of the obstacle, and the recirculation length does not increase when the distance l_0 is increased (see Fig. 11(a)). The recirculation size does increase with increasing Re , which corresponds with the flow past a single obstacle. The flow pattern is steady and symmetric with respect to the oncoming flow. When Re increases to greater than Re_{crit} , the steady flow becomes unstable and breaks into asymmetry,

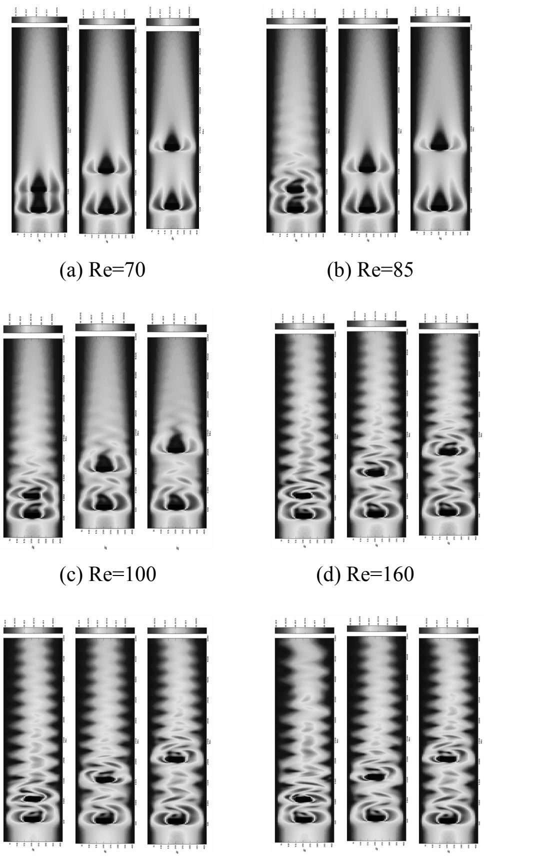

(a) Re=70 (b) Re=85

(c) Re=100 (d) Re=160

(e) Re=180 (f) Re=200

Fig. 12. Velocity profile around two square obstacles for Re=70,85,100,160,180,200 and various distance l_0, i.e., $l_0 = 50$ (left), $l_0 = 100$ (middle) and $l_0 = 150$ (right).

where the Re_{crit} differs from the Re_{crit} of the flow through one square obstacle. In our observation, asymmetrical flow occurs earlier in the case of $l_0 = 50$, which is around 75. It is less than the Re_{crit} of the flow past one square obstacle. Therefore, we can clearly show the asymmetrical flow for $\mathrm{Re} = 85$, which occurs before the other l_0 (see on the left side of Fig. 11(b)); but in the case of $l_0 = 100,\ 150$, the Re_{crit} occurs late at around 90. The flow seems to be a symmetrical flow and still a laminar flow (see Fig. 11(b) middle and right side). For $\mathrm{Re} > \mathrm{Re}_{crit}$, the flow becomes an asymmetrical and unstable flow. And, according to this result, the flow generated a periodicity of vortex shedding into the stream, as shown in Fig. 11(c)-(f).

We also examined this flow feature by visualizing the flow pattern through the velocity profile, as seen in Fig. 12. This figure shows the magnitude of the velocity field $|\vec{u}| = \sqrt{u^2 + v^2}$, as obtained from LB simulation. The flow pattern at low Re shows the laminar flow, which does not generate a vortex shedding pattern (see Fig. 12(a)). For $\mathrm{Re} = 85$, the visualization result of $l_0 = 50$ clearly illustrates the shedding pattern behind the obstacle, because the shedding is generated at around $\mathrm{Re} = 75$, while the shedding for the cases of $l_0 = 100$ and $l_0 = 150$ is shown in Fig. 12(b). The vortex shedding starts to appear earlier as the distance l_0 decreases (i.e., as the space between the obstacles becomes smaller) for a fixed Re. For $\mathrm{Re} > 85$, we found that the wake of the flow shows asymmetry due to a vortex shedding pattern behind the obstacle for every l_0, as presented in Fig. 12(c)-(f). There are two regions where the vortex shedding occurs: the space between the two obstacles (upstream obstacle) and the region behind the second obstacle (downstream obstacle). We found that the absence of vortex shedding in the wake of the upstream obstacle is mainly due to the small spacing between the two square obstacles (see the case of $l_0 = 50$), while vortex shedding does take place behind the wakes of both regions for $l_0 = 100$ and $l_0 = 150$. This observation indicates that the upstream obstacle controls the unsteady wake of the downstream obstacle. Since the flow velocity in front of the obstacle is mainly influenced by inter-obstacle spacing, it becomes a key parameter governing the generation of an unsteady flow.

To characterize the vortex shedding pattern behind the obstacle, we used the same scheme as we did when examining the flow past one square obstacle, which is to firstly calculate the frequency by using FFT of the time series data of the velocity profile in the wake of the downstream obstacle that clearly represents a periodic shedding pattern. The results of the time series data of the flow velocity evolution are shown in Fig. 13. The frequency of the signal shows a slight increase as the distance between the obstacles increases. Then, the variation of the St for various Re and different distances l_0 are shown in Fig. 14. We found that the St increases until it reaches the maximum value; after that it will decrease when Re increases. Furthermore, the maximum St occurs at $\mathrm{Re} \approx 160$ but has a different value. This feature, as expected, is similar to an isolated square obstacle in a uniform flow. A comparison of the St for the flow through one square obstacle and two square obstacles is then shown in Fig. 15, where it can be seen that all configurations have a similar feature with respect to the variation of Re for a fixed blockage ratio, although it has a different value.

Therefore, not only are Re and flow parameters crucial parameters to control the flow phenomena in the channel, but so are the number of the obstacles and their layout. In experimental practice, the flow through two square obstacles is usually more significant in the setup of the complexity inside the channel of many devices and hard to incorporate. Even if obstacles in the channel do not generate unsteady or turbulent flow at the low Reynolds number, they can stir the fluid to create lateral mass transport to improve the mixing performance. On the bright side, there seem to be more ways to generate unsteady or turbulent flow for two or more complex obstacles. The use of other intact devices such as the micro-oscillatory stirrer, or the employments of adjusted parameters such as the characteristic of the obstacle (irregular shapes), flow parameters, boundary conditions, and so on, could lead to increased mixing efficacy.

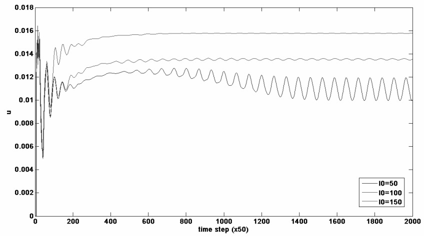

(a) Re=85

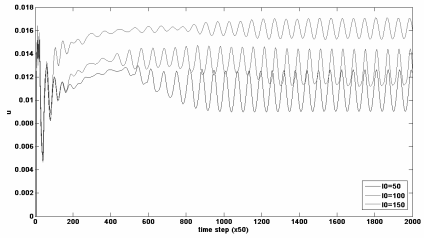

(b) Re=100

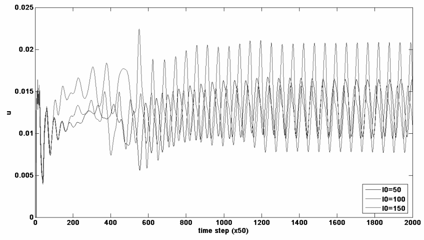

(c) Re=160

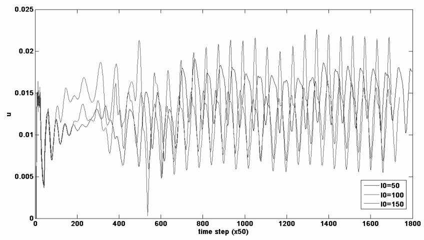

(d) Re=200

Fig. 13. Time series of the flow velocity for two obstacles at various distance l_0 for Reynolds number Re=85,100,160,200.

6. Concluding remarks

Mesoscopic modeling via a computational lattice Boltzmann method (LBM) approach was used to investigate flow pattern phenomena and the topology of vortex shedding behind one and two square obstacles with a fixed blockage ratio $\beta = 1/4$, centered inside a 2D channel, for an Re range from 1 to 300. Moreover, the effect of the layout of the obstacles in the flow past two square obstacles was compared with that of one square obstacle.

To generate reliable numerical results, the LBM was used to investigate the 2D flow around one and two square obstacles inside a channel with a fixed blockage ratio $\beta = 1/4$ for

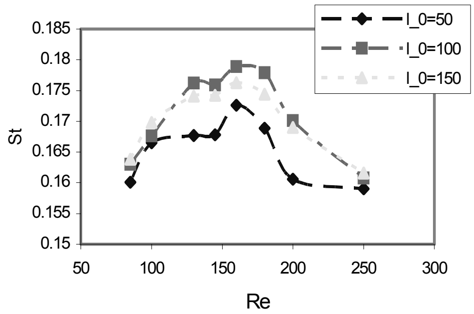

Fig. 14. Strouhal number for the flow around two obstacle for a range of Reynolds numbers $85 \le \mathrm{Re} \le 250$ for the various distance l_0.

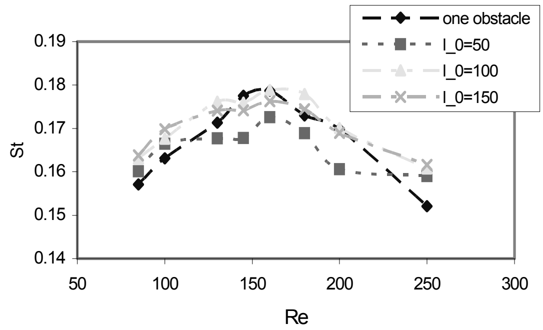

Fig. 15. Comparison of the Strouhal number for the flow around one and two obstacles.

a range of Reynolds number from 1 to 300. The flow behavior showed a steady flow for low Reynolds numbers and the symmetry breaks down and becomes an unstable flow for $\mathrm{Re} \ge \mathrm{Re}_{crit}$. According to the asymmetry of the flow and a sufficient number of iteration times, these flows become periodic and generate vortex shedding into the stream, which is known as a von Karman vortex street. The flow through one and two square obstacles has different characteristics regarding the periodicity of the vortex shedding. Consequently, the Strouhal number is used to characterize the shedding frequency of the flow, where the shedding frequency goes up as Re increases corresponding to the general behavior of St with Re. For two-obstacles, inter-obstacle spacing is identified as a key parameter controlling the nature of the unsteady flow and influencing the synchronization phenomena. From the chemical mixing viewpoint, $\mathrm{Re} \ge \mathrm{Re}_{crit}$ (which results in an unsteady or turbulent flow) is a practical condition for the chemical mixing process. Still other parameters such as the characteristic of the obstacle (irregular shapes), flow parameters, and boundary conditions could contribute to the holistic understanding of the mixing of chemicals. Potentially, more research needs to be done to obtain an optimal setup and operating condition for the mixing of microfluidic devices.

Acknowledgments

The authors thank David Blyler for editing the manuscript and providing helpful comments. This work is partially supported by the Center of Excellence for Innovation in Chemistry (PERCH-CIC), Thailand Center of Excellence in Physics (ThEP), Thailand Research Fund (TRF), Commission on Higher Education (CHE), and the Development Promotion of Science and Technology (DPST), Thailand.

Nomenclature

f_α : Distribution function
f_α^{eq} : Equilibrium distribution function
$\vec{e}_\alpha$: Discrete velocity
τ : Dimensionless relaxation time
ω_α : Weighting factor
ρ : Density
$\vec{u}$: Macroscopic velocity
p : Pressure
υ : Viscosity
H : Channel height
L : Channel length
l : Inflow length
l_0 : Distance between obstacles
d : Obstacle diameter
Nx : Number of grids in x direction
Ny : Number of grids in y direction
β : Blockage ratio
Re : Reynolds number
Re_{crit} : Critical Reynolds number
$u_{\max}$: Maximum flow velocity
St : Strouhal number
f : Characteristic frequency

References

[1] R. Davis and E. Moore, A numerical study of vortex shedding from rectangles, *J.Fluid Mech*. 116 (2006) 475-506.
[2] A. Mukhopadhyay, G. Biswas and T. Sundararajan, Numerical investigation of confined wakes behind a square cylinder in a channel, *Int. J. Num. Meth. Fluids*, 14 (12) (1992).
[3] H. Suzuki, Y. Inoue and T. Nishimura et al., Unsteady flow in a channel obstructed by a square rod (crisscross motion of vortex), *Int. J. Heat Fluid Flow*, 14 (1) (1993) 2-9.
[4] G. Wei-Bin, W. Neng-Chao and S. Bao-Chang et al., Lattice-BGK simulation of a two-dimensional channel flow around a square cylinder, *Chin. Phys*., 12 (2003) 67-74.
[5] P. Ratanadecho, Practical Aspects of the Simulation of Two-Dimensional Flow Around Obstacle with Lattice Boltzmann Method (LBM), *Tham. Int.J. Sci.Tech*., 8 (4) (2003).
[6] B. Carmo and J. Meneghini, Numerical investigation of the flow around two circular cylinders in tandem, *J. Fluids Struc*., 22 (6-7) (2006) 979-988.
[7] G. us Feedback, S. Ul Islam and CY Zhou, *Inf. Tech. J*., 8 (4) (2009) 513-520.
[8] H. Chen, S. Chen and W. H. Matthaeus, Recovery of the Navier-Stokes equations using a lattice-gas Boltzmann method, *Phys. Rev. A*, 45 (8) (1992) R5339.
[9] X. He and L.-S. Luo, A priori derivation of the lattice Boltzmann equation, *Phys. Rev. E*, 55 (6) (1997) R6333.
[10] G. R. McNamara and G. Zanetti, Use of the Boltzmann Equation to Simulate Lattice-Gas Automata, *Phys. Rev. Lett*., 61 (20) (1988) 2332.
[11] Y. Qian, D. d'Humieres and P. Lallemand, Lattice BGK models for Navier-Stokes equation, *Euro. Lett.*, 17 (6) (1992) 479-484.
[12] R. Benzi, S. Succi and M. Vergassola, The lattice Boltzmann equation: theory and applications, *Phys. Rep*., 222 (3) (1992) 145-197.
[13] S. Chen and G. Doolen, Lattice Boltzmann method for fluid flows, *Ann. Rev. Fluid Mech*., 30 (1) (1998) 329-364.
[14] R. Mei, L. Luo and W. Shyy, An accurate curved boundary treatment in the lattice Boltzmann method, *J. Comp. Phys*., 155 (2) (1999) 307-330.
[15] J. Bernsdorf, F. Durst and M. Sch fer, Comparison of cellular automata and finite volume techniques for simulation of incompressible flows in complex geometries, *Int. J. Num. Meth. Fluids*, 29 (3) (1999) 251-264.
[16] J. Zhou, *Lattice Boltzmann methods for shallow water flows*: Springer Verlag, 2004.
[17] X. He and L.-S. Luo, Theory of the lattice Boltzmann method: From the Boltzmann equation to the lattice Boltzmann equation, *Phys. Rev. E*, 56 (6) (1997) 6811.
[18] P. Kundu, *Fluid Mechanics*, 638 pp, Academic Press, 1990.
[19] C. Williamson, Vortex dynamics in the cylinder wake*, Ann. Rev. Fluid Mech*., 28 (1), (1996) 477-539.

Jiraporn Yojina received a Ph.D. in Applied Mathematics from the Mathematics Department, Mahidol University, Bangkok, Thailand, in 2010. Her research interests focus on mathematical biology and medicine.

Waipot Ngamsaad received a Ph.D. in Physics from Mahidol University, Bangkok, Thailand, in 2010. His research interests focus on computational biophysics and LBM.

Wannapong Triampo received a Ph.D. in Physics from Virginia Tech, USA, in 2001. Sinice graduation, he has been with Mahidol University, Thailand, where he is now an Associate Professor in Physics. His research interests focus on biophysics and stochastic modeling.